A Priori Surface Reflectance-Based Cloud Shadow Detection Algorithm for Landsat 8 OLI

Lin Sun, Quan Wang, Xueying Zhou, Jing Wei, Xu Yang, Wenhua Zhang, and Nan Ma

***Abstract*— Prior knowledge of the background land surface reflectance (LSR) constitutes one of the most important factors affecting the precision of cloud shadow detection. To resolve this problem, a surface reflectance-based cloud shadow detection (SRCSD) algorithm is proposed for multitemporal Landsat images. Monthly surface reflectance data sets constructed from MODIS surface reflectance products (MOD09A1) were used to provide the background LSR for cloud shadow detection. Based on the background LSR, the possible variation in the top of atmosphere (TOA) reflectance for each clear pixel can be estimated using the radiative transfer equation under different atmospheric conditions. If a pixel has a smaller TOA reflectance than the minimum value of the possible range under clear conditions, it is identified as being shadow covered. One hundred and twenty-five Landsat 8 Operational Land Imager scenes covered by various surface types were selected to evaluate the feasibility of the algorithm. A validation using manual cloud shadow masks showed that the average producer's accuracy and user's accuracy were approximately 0.805 and 0.893, respectively. A comparison of the results of the SRCSD algorithm with those of an object-based cloud shadow detection algorithm (Fmask) recently developed for Landsat images revealed that SRCSD generally detects cloud shadows better than Fmask. The most significant improvement of the SRCSD algorithm is the better detection capability for thin and broken cloud shadows, and this algorithm can be extended to multiple types of satellite data after proper modification.**

***Index Terms*— Cloud shadows, Fmask, Landsat 8 Operational Land Imager (OLI), surface reflectance-based cloud shadow detection (SRCSD).**

I. Introduction

COMPARED with previous Landsat instruments, the Landsat 8 Operational Land Imager (OLI), which exhibits an enhanced radiometric resolution of 12 bits, boasts greatly enhanced features, including the addition of a deep blue channel (band 1) and a new shortwave infrared channel (band 9) which is used to detect water resources, coastal zones, and cirrus clouds. These improvements, which significantly extend the application range of Landsat 8 OLI data, improve the accuracy of both the retrieval of biogeochemical properties and the identification of land cover. However, in the field of remote sensing, clouds and cloud shadows lead to numerous problems, including inaccurate atmospheric corrections, biased estimations of biogeochemical properties, and erroneous land cover classification and land cover change detection results [1]. In addition, the spectral signatures of cloud shadows can vary with the signal characteristics of the underlying surface, and the shadows of thin clouds can be brighter than the average surface reflectance due to the penetration of solar radiation [2]. Therefore, the detection of cloud shadows can be difficult.

Current cloud shadow detection algorithms can be mainly organized into two categories: threshold-based algorithms and matching-based algorithms. Threshold-based algorithms employ thresholds to separate shadow-covered observations from clear observations [3]–[5]. However, due to the complexity of the spectral characteristics of the land surface and especially of thin clouds, these methods encounter difficulties when selecting suitable thresholds.

Cloud shadows result from the projection of clouds onto the land surface. If a cloud is detected, the direction and area of the cloud shadow can be deduced according to the cloud height, solar azimuth, and zenith angle. Matching-based algorithms have been developed based upon this principle [6]–[8]. These methods are based on mathematical concepts that utilize a priori knowledge and geometric constraints to simulate the projection regions. However, most applications still contain restrictions due to elevation variations and time-consuming geometric cloud/shadow considerations, as elevation variations may cause errors in cloud height estimates.

To improve the cloud shadow detection performance using Landsat 8 OLI images, this paper proposes a surface reflectance-based cloud shadow detection (SRCSD) algorithm. Time series of global monthly surface reflectance data sets were constructed to calculate the potential apparent clear-sky reflectances by using the radiative transfer equation. Pixels with apparent reflectances lower than the possible minimum are identified as cloud shadows. The proposed approach is clearly distinctive from previous algorithms because it uses a dynamic threshold. In addition, this method does not depend on the cloud height, which may contain large errors.

II. Principle

The instrument-measured signals can be described as follows [9]:

$$L(\tau_a, \mu_s, \mu_v, \emptyset) = L_0(\tau_a, \mu_s, \mu_v, \emptyset) + \frac{\rho}{1 - s(\tau_a) \cdot \rho} \cdot F_d(\tau_a, \mu_s) T(\tau_a, \mu_v) \quad (1)$$

Manuscript received January 28, 2018; revised April 16, 2018 and May 20, 2018; accepted June 5, 2018. Date of publication July 4, 2018; date of current version September 26, 2018. This work was supported in part by the National Natural Science Foundation of China under Grant 41771408 and in part by the Shandong Provincial Natural Science Foundation, China under Grant ZR201702210379. *(Corresponding author: Quan Wang.)*

L. Sun, Q. Wang, X. Zhou, and X. Yang are with Geomatics College, Shandong University of Science and Technology, Qingdao 266590, China (e-mail: sunlin6@126.com; wangquan_rs@hotmail.com; zhouxueying666@hotmail.com; xu_yang666@126.com).

J. Wei is with the Department of Earth System Science, Tsinghua University, Beijing 100084, China (e-mail: weijing_rs@163.com).

W. Zhang is with the College of Geography and Tourism, Qufu Normal University, Rizhao 276826, China (e-mail: zhangwenhua0426@163.com).

N. Ma is with the College of Physics and Electronics, Shandong Normal University, Jinan 250358, China (e-mail: manan1@stu.sdnu.edu.cn).

Color versions of one or more of the figures in this letter are available online at http://ieeexplore.ieee.org.

Digital Object Identifier 10.1109/LGRS.2018.2847297

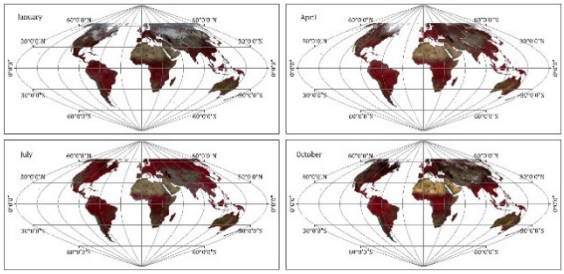

Fig. 1. Global monthly surface reflectances produced from the MOD09A1 product for January, April, July and October in 2014.

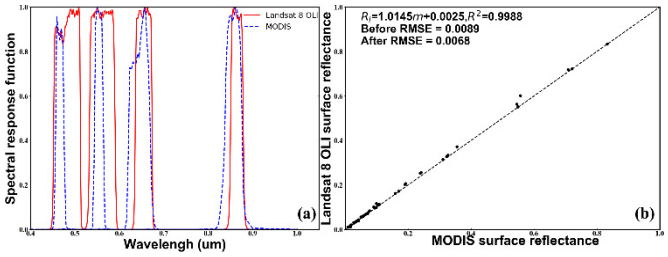

Fig. 2. (a) MODIS and Landsat 8 OLI spectral response functions. (b) Comparison of the surface reflectances in the blue band between MODIS and Landsat 8 OLI.

where $L(\tau_\alpha, \mu_s, \mu_v, \emptyset)$ is the top of atmosphere (TOA) reflectance; $L_0(\tau_\alpha, \mu_s, \mu_v, \emptyset)$ is the upward radiance of the atmosphere for a zero surface reflectance (referred to as the path radiance); $F_d(\tau_a, \mu_s)$ and $T(\tau_a, \mu_v)$ are the downward and upward atmospheric hemispherical reflectances, respectively; μ_s and μ_v are the cosines of the solar zenith angle (SZA) and view zenith angle (VZA), respectively; and τ_α is the aerosol optical depth (AOD).

From (1), the TOA reflectances of shadow-covered observations will be much lower than those of clear-sky observations due to a reduced value of $F_d(\tau_a, \mu_s)$. However, when semitransparent clouds are present, the reflectances of cloud shadows over bright surfaces (e.g., snow) at visible wavelengths or vegetation at near-infrared (NIR) wavelengths can still be highly affected by the penetration of solar radiation. Therefore, it is not easy to accurately distinguish shadow-covered from clear-sky observations, especially when the shadows are cast by thin clouds. However, if we know the prior LSR for each observation, the possible TOA reflectance range for clear observations can be estimated via (1) under common atmospheric conditions. The clear-sky/shadow-covered status for each observation is determined by a comparison with this possible range. If an observation exhibits a TOA reflectance that is lower than the possible range, the observation is more likely shadow-covered.

III. Methodology

A. Construction of the Prior Land Surface Reflectance Data Sets

MODIS surface reflectance products (MOD09) provide ground-level surface spectral reflectance measurements that exclude the impacts of atmospheric scattering and absorption. Each pixel in the MOD09A1 product, which is an 8-day gridded level-3 surface reflectance product with 500-m spatial resolution, contains the best possible level-2 gridded observation selected on the basis of high observational coverage, low viewing angle, absence of clouds or cloud shadows, and aerosol loading [10].

Bands 1–4 from MOD09A1 surface reflectance observations in 2013–2016 were selected to construct global monthly data sets as inputs for the cloud shadow detection. The second lowest surface reflectance value among all of the images in a given month was chosen to further reduce the impacts of clouds and cloud shadows. Fig. 1 displays the Red-Green-Blue (RGB) composition of channels 2, 1 and 4 for January, April, July, and October in 2014.

TABLE I

Transformation Parameters for Each Channel

Bands	a	b	RMSE (before correction)	RMSE (after correction)
Blue	1.0145	0.0025	0.0089	0.0068
Green	1.0024	0.0012	0.0078	0.0076
Red	1.0051	-0.0004	0.0041	0.0038
NIR	0.9997	0.0005	0.0032	0.0031

B. Transformation of the MODIS LSR to the Landsat 8 OLI LSR

Fig. 2(a) shows the spectral response function for each Landsat 8 OLI and MODIS band used for the detection of cloud shadows. Significant differences that might cause differences in the LSRs for the same target are detected among each band. Therefore, to identify cloud shadows with a high precision, it is necessary to convert the MODIS LSR to the Landsat 8 OLI LSR.

To transform the MODIS LSRs into Landsat 8 OLI LSRs, the spectral curves of 18 plants, 14 artificial materials, 9 liquids, and 13 soils with wavelengths ranging from 400 to 1000 nm were obtained from the United States Geological Survey (USGS) spectral library [11]. The relationships between individual measured spectra and the corresponding surface reflectance of each sensor were analyzed based on the following equation [12]:

$$\rho = \frac{\int_{\lambda_1}^{\lambda_2} S(\lambda) \times \rho_r(\lambda) d\lambda}{\int_{\lambda_1}^{\lambda_2} S(\lambda) d\lambda} \tag{2}$$

where ρ is the surface reflectance for each band used for the detection of cloud shadows; $S(\lambda)$ is the spectral response function; and $\rho_r(\lambda)$ is the observed spectral reflectance obtained from the USGS spectral library. As shown in Fig. 2(b), the derived MODIS LSRs agree well and exhibit an obvious linear relationship with the Landsat 8 OLI LSRs in the blue channel. Thus, the Landsat 8 OLI LSRs can be retrieved from the MODIS LSRs accordingly

$$\rho_L = a \cdot \rho_M + b \tag{3}$$

where ρ_L and ρ_M are the Landsat 8 OLI and MODIS LSRs, respectively, and a and b are two coefficients.

Table I illustrates the linear transformation results. The surface reflectance correction results reveal the root mean square error (RMSE) was effectively reduced, indicating that the error was properly corrected.

C. Threshold Calculation for the Detection of Cloud Shadows

In the absence of the effects of clouds and cloud shadows, the TOA reflectance for a known LSR has a definite range under normal atmospheric and observational conditions. Accordingly, the Second Simulation of the Satellite Signal in the Solar Spectrum (6S) model was used to simulate the variability in TOA reflectance values under different atmospheric and observational conditions over surface targets [13].

With respect to the parameters of simulated processes, different types of atmospheric and aerosol models are considered. Changes in the TOA reflectance according to the LSR are simulated from the AOD variations (varying from 0.1 to 0.6 with a step of 0.1) and various geometrical conditions (the SZA varying from 10° to 55° with a step of 15° and the VZA varying from 10° to 40° with a step of 10°). The presence of cloud shadows will drastically reduce the observed TOA reflectance. Therefore, the minimum value of the derived TOA reflectance distribution can be simulated as a function of the surface reflectance and observational geometry to differentiate shadow-covered observations from clear-sky observations:

$$T_{\text{blue}} = 0.6410 \times \rho_L + 0.0336 \cdot \cos\alpha \cos\beta + 0.0299 \quad (4)$$

$$T_{\text{green}} = 0.6555 \times \rho_L + 0.0187 \cdot \cos\alpha \cos\beta - 0.0079 \quad (5)$$

$$T_{\text{red}} = 0.7289 \times \rho_L + 0.0121 \cdot \cos\alpha \cos\beta - 0.0201 \quad (6)$$

$$T_{\text{NIR}} = 0.8324 \times \rho_L + 0.0059 \cdot \cos\alpha \cos\beta - 0.0930 \quad (7)$$

where T_{blue}, T_{green}, T_{red}, and T_{NIR} are the minimum TOA reflectances for the blue, green, red, and NIR bands, respectively; ρ_L is the transformed surface reflectance; and α and β are the SZA and VZA, respectively.

Due to differences in the spatial resolution, a search is conducted for the surface reflectance of a Landsat 8 OLI pixel within the corresponding monthly surface reflectance data set according to the geographic coordinates of the pixel center. In the SRCSD algorithm, if the TOA reflectance of a pixel is below the minimum possible range of the TOA reflectance calculated with the surface reflectances under different observational and atmospheric conditions, the pixel is identified as a potentially shadow-covered observation, and a shadow-covered observation is identified only if it contains a cloud shadow in all four band tests

$$R_i = R_o < T_i (\text{i} = \text{blue, green, red, NIR}) \quad (8)$$

$$R = R_{\text{blue}} \cap R_{\text{green}} \cap R_{\text{red}} \cap R_{\text{NIR}} \quad (9)$$

where R_i is the result in a given channel; T_i denotes the minimum TOA reflectances for the blue, green, red, and NIR bands; R_o is the observed value; R is the output result; and R_{blue}, R_{green}, R_{red}, and R_{NIR} are the results in the blue, green, red, and NIR bands, respectively.

IV. Experiment and Verification

A. Comparison with the Fmask Method

A total of 125 Landsat 8 OLI images over different surface types within the 2013–2016 period were selected for experimentation to evaluate the feasibility of the SRCSD algorithm. Furthermore, cloud shadows cast by thin, thick, and broken clouds over several typical surface types (i.e., soil, vegetation, desert, soil, and water) were selected to validate the accuracy of the proposed approach.

To highlight the superiority of the SRCSD method, the SRCSD results were compared with those obtained by the Fmask algorithm, in which cloud shadows are initially extracted based on a flood-fill transformation and then confirmed based on an object-based cloud and cloud shadow matching approach [2], [7]. For each comparison shown, the Fig. 3 (left) displays the standard false color composite Landsat image, while the Fig. 3 (middle) and (right) are the results of the SRCSD and Fmask algorithms, respectively (black: clear sky; white: clouds; and gray: cloud shadows).

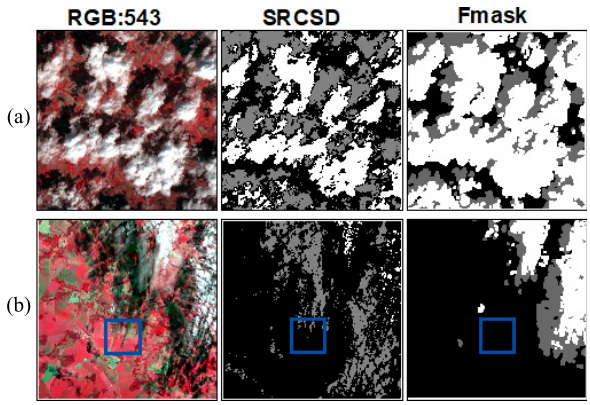

Fig. 3. Comparison of the SRCSD and Fmask results for Landsat tiles over vegetated areas. (Left) Standard false color composite images. (Middle) SRCSD results. (Right) Fmask results. Black: clear sky. White: clouds. Gray: cloud shadows. (a) Thick cloud shadows over densely vegetated area. (b) Thin cloud shadows over cropland.

Fig. 3(a) and (b) shows a comparison of the cloud shadow masks over vegetated areas generated by the SRCSD and Fmask algorithms. According to Fig. 3(a), both the SRCSD algorithm and the Fmask algorithm can accurately detect thick cloud shadows due to their relatively darker reflectances, as the spectral characteristics of the cloud shadows differed significantly from those of the vegetation. However, the Fmask method may erroneously identify cloud shadows as clouds, because it expanded all of the clouds by three pixels in all eight connected directions. Fig. 3(b) shows that the SRCSD algorithm can also accurately identify the thin cloud shadows over cropland using short-period references; that is, the changes in the cropland reflectance during the growth season are much slower than those of cloud shadows. However, the Fmask technique cannot match the shadows of thin, high clouds. Moreover, the incredibly thin cloud shadows located within the blue rectangle (Fig. 3) are too thin; therefore, the TOA reflectance does not differ significantly from the model-estimated values. Unfortunately, this omission is usually not avoidable in the SRCSD algorithm.

Fig. 4 shows the cloud shadow masks generated by the SRCSD and Fmask algorithms for broken and thin clouds over desert and bare soil. The reflectances of the clear-sky observations over bright surfaces were much larger than those of the shadow-covered observations; the reflectances decreased dramatically when cloud shadows were present, and therefore, it was easy to find an extreme point to differentiate the image [Fig. 4(a)]. In addition, when the clouds are semitransparent, the darkening effects of the cloud shadows are subtle; consequently, the reflectances of the thin cloud shadows over bright surfaces were higher than those of general objects and similar to the surroundings [Fig. 4(b)]. The SRCSD method is a pixel-based algorithm, and thus, it identified very small and thin cloud shadows that are often misidentified by object-based algorithms (Fmask).

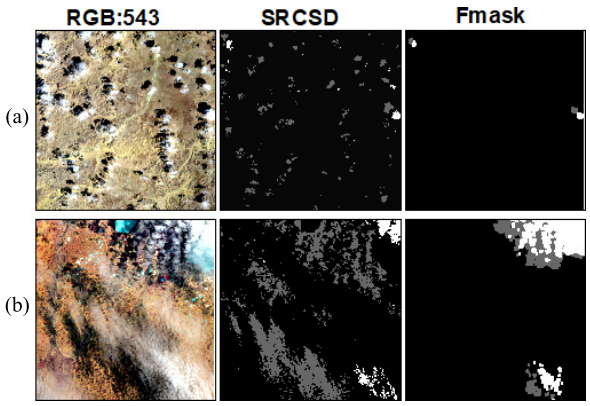

Fig. 4. Comparison of the SRCSD and Fmask results for Landsat tiles over a bright area. (a) Broken cloud shadows over desert. (b) Thin cloud shadows over desert.

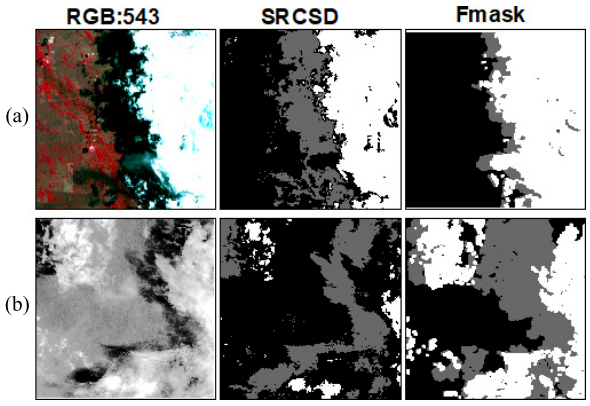

Fig. 5. Comparison of the SRCSD and Fmask results for Landsat tiles over vegetated and water areas. (a) High cloud shadows over a sparsely vegetated area. (b) Thin cloud shadows over a water area.

Fig. 5 shows the cloud shadows identified using the SRCSD and Fmask algorithms over sparse vegetation and water. Although slight differences existed between the water and shadow-covered observations, the SRCSD algorithm was able to effectively distinguish most of the cloud shadows over water using a single blue band [Fig. 5(b)]. The Fmask algorithm assumes that a maximum match similarity exists between clouds and their shadows. However, dark objects that exist between the clouds and their shadows can complicate the matching of clouds with their associated cloud shadows in the Fmask algorithm, and consequently, cause errors in the cloud shadow identification (Fig. 5).

The Fmask algorithm failed to identify shadow-covered observations due to false matches in some regions, especially on the edges of scenes in which the clouds were absent [Fig. 6(a)] or where the cloud results were incorrect [Fig. 6(b)]. However, the pixel-based SRCSD algorithm successfully distinguished these kinds of shadows using the differences in the TOA reflectances between the clear-sky and shadow-covered observations.

B. Accuracy Assessment of SRCSD

Forty-one tiles covering several typical land types were chosen to quantitatively analyze and demonstrate the performance of the SRCSD algorithm. Two pairs of comparisons

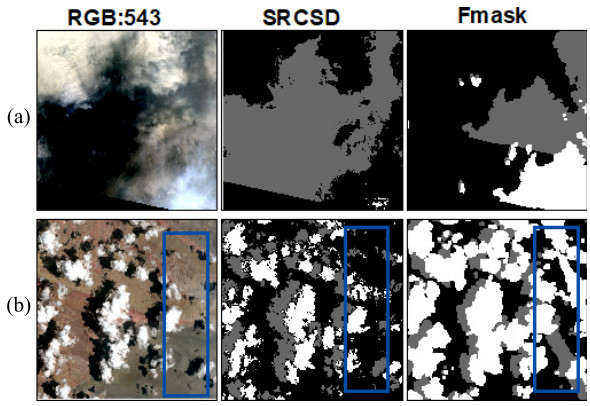

Fig. 6. Comparison of the SRCSD and Fmask results for Landsat tiles over bare soil. (a) Thin cloud shadows at the edge of the scene. (b) Thick cloud shadows over a bare soil area.

are presented to illustrate the accuracy: one pair comprises SRCSD results and manual cloud shadow masks, and the second pair is composed of cloud shadow masks from the SRCSD and Fmask algorithms. Each observation from each pair of masks was labeled as belonging to one of seven categories: shadow-covered by both methods (hereafter referred to as ShadowBoth); clear sky by both methods (hereafter referred to as ClearBoth); clear sky by the manual mask and SRCSD algorithm (hereafter referred to as ClearM and ClearS, respectively); shadow covered by the manual mask (hereafter referred to as ShadowM); shadow covered by the SRCSD algorithm (hereafter referred to as ShadowS); and shadow-covered by the Fmask algorithm (hereafter referred to as ShadowF). Five indices (10)–(13) were chosen as indicators for the accuracy assessment

$$\mathrm{PA} = \frac{\mathrm{ShadowBoth}}{\mathrm{ShadowM}} = 1 - \mathrm{Omission\ Error} \tag{10}$$

$$\mathrm{UA} = \frac{\mathrm{ShadowBoth}}{\mathrm{ShadowS\ or\ ShadowF}} = 1 - \mathrm{Commission\ Error} \tag{11}$$

$$\mathrm{SumPro} = \mathrm{ShadowM} \cdot \mathrm{ShadowS} + \mathrm{ClearM} \cdot \mathrm{ClearS} \tag{12}$$

$$\mathrm{KHAT} = \frac{\mathrm{Total\ Pixels} \cdot (\mathrm{ClearBoth} + \mathrm{ShadowBoth}) - \mathrm{SumPro}}{\mathrm{Total\ Pixels}^2 - \mathrm{Sumpro}} \tag{13}$$

where Total Pixels is the total number of pixels in the tile, KHAT is an estimate of kappa analysis.

Fig. 7 shows the different indicators used for the accuracy assessment of the SRCSD algorithm. The total counts of ShadowM and ShadowS were calculated, and the percentage distributions of the shadow-covered observations with both the manual masks and the SRCSD algorithm are displayed. The ShadowS observations were relatively smaller than the ShadowM observations. The slope and intercept of the regression equation were 0.96 and 0.005, respectively. The R^2 value was 0.9111, and the RMSE was 0.0175, indicating that the shadow-covered observations from the SRCSD algorithm are reliable. The average KHAT was 0.8202. These results reveal that the SRCSD algorithm results have good agreement with the results of the manual masks. To further affirm the accuracy of the SRCSD algorithm, the producer's accuracy (PA) and user's accuracy (UA) from the SRCSD and Fmask results were selected for comparison. The average PA from the SRCSD

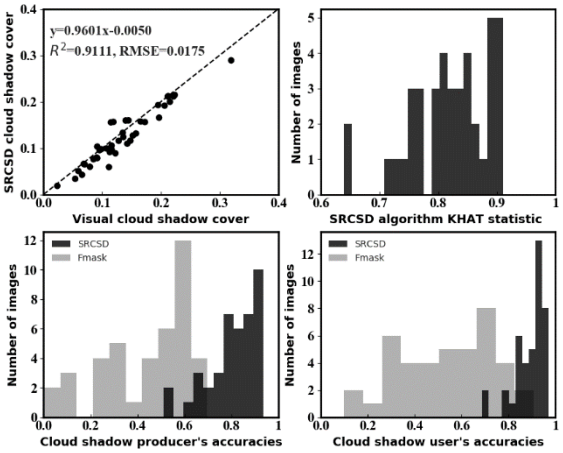

Fig. 7. Accuracy assessment for the SRCSD algorithm. (Top left) Agreement between the SRCSD results and manual masks. (Top right) Kappa analysis of the SRCSD algorithm. (Bottom) Comparison between the SRCSD and Fmask algorithms in terms of the PA and UA.

results (0.8051) was significantly larger than that from the Fmask results (0.4405), and the mean UA for SRCSD (0.8926) was much higher than that for Fmask (0.5350), suggesting that the clear-sky observations from SRCSD were misidentified less often than those from Fmask. The bias distributions of the PA and UA suggest that the cloud shadow masks from the SRCSD algorithm are superior to those from the Fmask algorithm.

V. Conclusion

An algorithm was developed to detect cloud shadows in Landsat 8 OLI images supported by prior LSR data sets. The minimum values of the Landsat 8 OLI TOA reflectance for a certain LSR were simulated using the 6S model under normal atmospheric conditions. On that basis, a threshold calculation model was constructed and used to differentiate shadow-covered and clear-sky observations.

The SRCSD algorithm was applied to Landsat 8 OLI images to generate cloud shadow masks over different types of underlying surfaces and then compared with the Fmask method. The results showed that the SRCSD algorithm performed better than the Fmask algorithm, especially when used to identify broken cloud shadows and thin cloud shadows over different land types. The error matrix indicated that approximately 81% of the shadow-covered observations in the images were correctly distinguished, while only approximately 11% of the shadow-covered observations from the SRCSD algorithm were misidentified.

There are three potential problems in the proposed approach. First, sudden changes in the surface type could lead to a mismatch in the surface type, thereby producing significant changes in the LSR and leading to erroneous shadow recognition results. However, changes in surface types, such as urban expansion and deforestation, are usually slow processes, and in the future work, these errors can be reduced by shortening the update period of the prior LSR data sets. Second, spatial matching errors between the LSR data and Landsat 8 OLI TOA reflectance data may lead to linear distributions of objects that are misidentified as cloud shadows. Improving the matching accuracy and the prerecognition of linear objects will help reduce such errors. Third, complicated conditions, such as extremely thin cloud shadows and heavy aerosols, may exist. The SRCSD algorithm may not be able to identify some extremely thin cloud shadows that are not sufficiently dark for identification as cloud shadows; however, these cloud shadows will not pose highly serious problems for most remote sensing activities. Meanwhile, heavy aerosols will diffuse within cloud shadows and cause them to exhibit reflectances that are even higher than the minimum values. Unfortunately, this kind of omission is usually not avoidable.

Acknowledgment

The authors would like to thank the National Aeronautics and Space Administration website for providing the Landsat 8 OLI data and MOD09A1 data. They would also like to thank Z. Zhu and C. E. Woodcock for providing the codes for the Fmask algorithm.

References

[1] L. Sun *et al.*, "A cloud detection algorithm-generating method for remote sensing data at visible to short-wave infrared wavelengths," *ISPRS J. Photogram. Remote Sens.*, vol. 124, pp. 70–88, Feb. 2017.

[2] Z. Zhu and C. E. Woodcock, "Automated cloud, cloud shadow, and snow detection in multitemporal Landsat data: An algorithm designed specifically for monitoring land cover change," *Remote Sens. Environ.*, vol. 152, pp. 217–234, Sep. 2014.

[3] M. Derrien and H. L. Gléau, "Improvement of cloud detection near sunrise and sunset by temporal-differencing and region-growing techniques with real-time SEVIRI," *Int. J. Remote Sens.*, vol. 31, no. 7, pp. 1765–1780, Apr. 2010.

[4] R. Richter and A. Müller, "De-shadowing of satellite/airborne imagery," *Int. J. Remote Sens.*, vol. 26, no. 15, pp. 3137–3148, Aug. 2005.

[5] S. Martinuzzi, W. A. Gould, and O. M. R. González, "Creating cloud-free Landsat ETM+ data sets in tropical landscapes: Cloud and cloud-shadow removal," U.S. Dept. Agriculture, Forest Service, Int. Inst. Tropical Forestry, San Juan, Puerto Rico, Tech. Rep. IITF-32, 2007, vol. 32.

[6] N. R. Goodwin, L. J. Collett, R. J. Denham, N. Flood, and D. Tindall, "Cloud and cloud shadow screening across Queensland, Australia: An automated method for Landsat TM/ETM + time series," *Remote Sens. Environ.*, vol. 134, pp. 50–65, Jul. 2013.

[7] Z. Zhu and C. E. Woodcock, "Object-based cloud and cloud shadow detection in Landsat imagery," *Remote Sens. Environ.*, vol. 118, pp. 83–94, Mar. 2012.

[8] B. Zhong, W. Chen, S. Wu, L. Hu, X. Luo, and Q. Liu, "A cloud detection method based on relationship between objects of cloud and cloud-shadow for Chinese moderate to high resolution satellite imagery," *IEEE J. Sel. Topics Appl. Earth Observ. Remote Sens.*, vol. 10, no. 11, pp. 4898–4908, Nov. 2017.

[9] S. Liang, "Narrowband to broadband conversions of land surface albedo I: Algorithms," *Remote Sens. Environ.*, vol. 76, no. 2, pp. 213–238, May 2001.

[10] E. Vermote, S. Kotchenova, and J. Ray, "MODIS surface reflectance user's guide, version 1.4," MODIS Landsat Surface Reflectance Science Comput. Facility, College Park, MD, USA, 2015. [Online]. Available: http://modis-sr.ltdri.org

[11] R. F. Kokaly *et al.*, "USGS spectral library version 7," U.S. Geological Surv., Reston, VA, USA, Tech. Rep. 1035, Apr. 2017. [Online]. Available: http://pubs.er.usgs.gov/publication/ds1035

[12] D. A. Rutan and T. P. Charlock, "Spectral reflectance, directional reflectance, and broadband albedo of the Earth's surface," in *Proc. 9th Conf. Atmos. Radiat.*, Boston, MA, USA, vol. 9, 1997, pp. 466–470.

[13] E. Vermote, D. Tanré, J. L. Deuzé, M. Herman, J. J. Morcrette, and S. Y. Kotchenova. *Second Simulation of a Satellite Signal in the Solar Spectrum–Vector (6SV)*. Accessed: Apr. 2, 2018. [Online]. Available: http://6s.ltdri.org/pages/manual.html